Biomechanical and optical behavior of human corneas before and after photorefractive keratectomy

Paolo Sánchez, MS, Kyros Moutsouris, MD, Anna Pandolfi, PhD

Laser refractive corneal surgery for the correction of vision defects has become popular, and its use continues to increase. Scientific research, technology, and the design of new instruments to improve refractive errors have drawn the attention of specialized physicians, physicists, engineers, and opticians. The probability of a successful intervention increases with the reliability of sophisticated surgical instruments and the availability of accurate nomograms.[1] Nevertheless, additional predictive tools based on numerical models of the eye that simulate different phases of surgery can be useful to the surgeon, in particular for corneas with topography anomalies and irregularities.[2]

A numerical model of the eye consists of a geometrical model and a material model. The geometrical model describes the shape of the anterior and posterior surfaces of the cornea because the refractive power is connected to the lens curvature. The material model describes the mechanical behavior of the stroma (the thickest layer of the cornea with evident bearing functions). The material model must be able to reproduce the experimental evidence, and it must be characterized by algorithmic robustness and computational efficiency. Noninvasive imaging techniques, such as optical coherence tomography, capture digital images of the exact geometry of the cornea under the action of the physiologic intraocular pressure (IOP) (average

approximately 16 mm Hg) and record the corneal deformation resulting from the application of brief, localized air pressure. The knowledge of the mechanical response of the cornea to known actions, for example in the form of a sequence of images reproducing different phases of the deformation, is fundamental for the calibration of advanced material models that describe the micromechanical structure of the stroma.

In recent years, several material models have been developed for or adapted to the behavior the stromal tissue. These include models that account for the different components of the lamella (collagen fibrils, extrafibrillar matrix, and proteoglycans),[3] models that emphasize the presence of 2 sets of fibrils,[4] viscoelastic models,[5] models with distributed orientation of fibers for 2-dimensional (2-D)[6–8] or 3-dimensional (3-D) tissues,[9,10] and models including the uncrimping of collagen.[11] Material models for the stroma must account for quasi-incompressibility, anisotropy, and spatial distribution of the orientation of the collagen fibrils with different degrees of dispersion according to the location in the cornea. Recent studies[12–14] discuss advanced approaches for the evaluation of the mechanical properties of the cornea. In particular, Studer et al.[15] state that complex multiparameter models calibrated over a limited set of data might be misleading.

The use of numerical models—in particular those based on finite-element discretization—for the simulation of the mechanical behavior of the human cornea began in the late 1990s. The first examples of calculations combined inflation experiments and numerical simulations using linear elasticity and 2-D models.[16] Tridimensional models of the cornea using nonlinear elasticity and including anisotropy were developed to simulate keratoconus[17,18] and laser refractive surgery.[4,19,20] The availability of advanced numerical methods also allows for qualitative comparisons between the preoperative and postoperative behavior of the cornea,[21] estimation of the influence of material models[22] and of geometrical and material parameters[23] on the mechanical response of the cornea, simulation of advanced astigmatism correction procedures,[24] and real-time simulation of surgery by reduced-order modeling.[25] Most published material refers to ideal geometries and material models calibrated on average experimental data. Often, the experimental data are taken directly from the literature and the numerical simulations are purely qualitative, nullifying the possibility of being predictive. Recent numerical studies point out the need to use the correct geometry and the corresponding material properties in view of reliable simulations. A study of porcine corneas[26] proved that sole knowledge of the cornea geometry does not permit the prediction of the overall mechanical behavior and that once the material model is chosen, every single simulation requires accurate calibration of the patient-specific material properties. In the past, patient-specific finite element simulations of refractive and cataract surgery have been published.[15,21] The results show that given the exact geometry of a patient's eye, the corresponding material properties should be calibrated using nondestructive tests. If individual in vivo tests are missing, help in the choice of the material properties can be sought by considering the inevitable link between mechanics and optics.[20,22,27]

The aim of the present study was to assess the ability of an improved patient-specific version of a finite-element code[4,20] in predicting the optical and biomechanical outcomes of RK, in particular the corrected refractive power and the postoperative stress distribution in the treated corneas. The current version of the finite-element code includes a procedure that replicates the typical corneal ablation in PRK[20] and uses improved models of statistically distributed fiber materials.[10] Several recent studies[28–30] discuss including the description of the fibril organization in the human cornea. The material model used in the present calculations was proved to be sufficiently accurate, robust, and efficient. For the sake of convenience, we used our numerical model of the cornea and a material model developed in our group because of the awareness of the features of the code and the large variety of output data.

PATIENTS AND METHODS

This study comprised patients ranging in age from 20 to 40 years in whom PRK for myopic or myopic compound astigmatism was performed between 2007 and 2009 at Athineum Refractive Center, Athens, Greece. All patients returned for a 3-month follow-up. Preoperative and short-term postoperative corneal topographic maps were available and were used to set up patient-specific numerical simulations.

Submitted: August 23, 2013.
Final revision submitted: March 13, 2014.
Accepted: March 15, 2014.

From the Department of Biomechanical Engineering (Sánchez), Technical University, Delft, the Netherlands; the Athineum Refractive Center (Moutsouris), Athens, Greece; the Dipartimento di Ingegneria Civile e Ambientale, Politecnico di Milano (Pandolfi), Milan, Italy.

Corresponding author: Anna Pandolfi, PhD, Dipartimento di Ingegneria Civile e Ambientale, Politecnico di Milano, Piazza Leonardo da Vinci 32, 20133 Milano, Italy. E-mail: anna.pandolfi@polimi.it.

A preliminary examination was performed in all eyes to exclude atypical geometry or the presence of pathology characterized by reduced mechanical properties. Eyes with asymmetric topography or keratoconus suspect were excluded.

Preoperatively, a comprehensive ophthalmologic examination was performed. The evaluation included logMAR uncorrected distance visual acuity and corrected distance visual acuity, manifest refraction (sphere and cylinder), slitlamp biomicroscopy, Goldmann tonometry, fundus examination, central corneal thickness (CCT) measured by ultrasound (US) pachymetry, and corneal topographic and aberrometric analysis using the Orbscan II scanning-slit corneal topographer and software (Bausch & Lomb). Three months postoperatively, another comprehensive ophthalmologic examination was performed that included US pachymetry and corneal topographic and aberrometric analysis.

Surgical Technique

The same experienced surgeon (K.M.) performed all PRK procedures using the Amaris excimer laser (Schwind eye-tech-solutions GmbH and Co. KG) and a wavefront-optimized ablation profile. The intraoperative data included the ablation depth, optical zone, residual stromal bed, and ablation ratio, calculated as the ratio between the ablation depth and the CCT.

After epithelial debridement, the excimer laser ablation was performed using the pupil center under mesopic conditions as a center reference. Mitomycin-C 0.02% was administered for 30 seconds on the exposed corneal bed. Finally, a soft contact lens was placed and maintained until reepithelialization was complete (from 4 to 6 days). Topical tobramycin and dexamethasone eyedrops were used postoperatively every 6 hours for 1 week. Topical lubricants were given every 6 hours for 1 month.

Corneal Topography

The study evaluated corneal topography maps of the geometry of the human cornea at the physiologic configuration, when the organ is characterized by internal stresses that balance the action of the IOP. The Orbscan II scanning-slit corneal topographer uses an illuminated ring pattern and a beam of light across the cornea. The image sensors acquire the geometry of more than 9000 points on the corneal surface. The software produces several color maps describing relative elevation of the anterior surface of the cornea with respect to the anterior best-fit sphere (BFS), relative elevation of the posterior surface with respect to the posterior BFS, pachymetry, and axial refractive power. The axial refractive power map is built by using locally Snell's law as follows:

$$RP = \frac{n_{co} - 1}{R^{ant}} + \frac{n_{aq} - 1}{R^{pos}} \quad (1)$$

where RP is the refractive power, $n_{co} = 1.3375$ is the refractive index of the cornea, $n_{aq} = 1.336$ is the refractive index of the humor aqueous, and R^{ant} and R^{pos} are the best approximation within the optical zone of the distance measured along the line orthogonal to the anterior and posterior corneal surface, respectively, from the ocular axis. The refractive power is expressed in diopters ($D = m^{-1}$).

In addition to the global maps, the scanning-slit corneal topographer's output includes the main geometric parameters of the cornea. Of the parameters, this study used the radius of the BFS, white-to-white (WTW) distance, minimum and the maximum thicknesses at the limbus, refractive power, and orientation of the steepest and the flattest meridia. To verify rapidly the shape of the corneal geometry, an approximation of the anterior curvatures at the corneal apex in the direction of the 2 principal meridia (ie, R_s and R_f) was computed by inputting into equation 1 the maximum and minimum values of refractive power for the anterior surface and the BFS value of the posterior surface. Vice versa, from the numerical geometry of the cornea, the curvature along the principal meridia can be evaluated and the corresponding refractive power computed directly using equation 1.

It is well known that the Orbscan II topographer is not the best and most up-to-date instrument for acquiring the topology of the eye. In particular, the topographer's measurement precision is limited to the central 3.0 mm optical zone and its accuracy in capturing the shape of the posterior corneal surface, especially after PRK, is a potential limitation. The Orbscan II typically shows posterior surface changes that are not observed with other imaging modalities and more accurate measurements can be considered.[31–35] In the present work, it was decided to use the data from the instrument because the information was sufficient for the study's goal, although the model results may differ from the ones obtained with more sophisticated instruments because of differences in posterior surface data between imaging devices. In this study, corneal maps of refractive power were not produced; rather, a selected number of meridia were considered and the refractive power was computed using the best approximating circumference in the central optical zone. According to preliminary numerical tests, the larger influence on the mechanical response of the cornea in this study's model was due to the boundary conditions at the limbus, which affect the actual deformed geometry of the corneal periphery region. The direct influence on the mechanical response of the cornea on the limbus thickness and of the stress-free shape of the corneal periphery, which is thicker and less deformable with respect to the central zone, as well as the assumed fibril circumferential organization at the limbus appeared to have less influence than the limbus boundary conditions.[22]

Geometric Model

The numerical model of the cornea was first presented by Pandolfi et al.[20] The cornea is a thin dome-shaped shell connected to the white sclera through the limbus. The 3.0 mm radius central zone, called the optical zone, is responsible for the correct focusing of light rays on the retina. The optimum shape for the optical zone is a spherical cap; however, such a shape is very unlikely in human eyes, in which small deviations from perfect sphericity are normal. An accurate description of the shape of the anterior and posterior surfaces of the cornea is given by biconic equations,[28] whose parameters can be easily evaluated by best fitting the set of points acquired by the scanning-slit corneal topographer's system. An explicit biconic equation in a cylindrical reference system (ρ,θ, z) is given by

$$z\left(\rho, \theta; R_s, R_f, Q_s, Q_f, \alpha, z_0\right) = z_0 - \frac{\rho^2 A}{1 + \sqrt{1 - \rho^2 B}} \quad (2)$$

where

$$A = \frac{\cos^2(\theta - \alpha)}{R_s} + \frac{\sin^2(\theta - \alpha)}{R_f}$$

$$B = (Q_s + 1)\frac{\cos^2(\theta - \alpha)}{R_s^2} + \left(Q_f + 1\right)\frac{\sin^2(\theta - \alpha)}{R_f^2}$$

In equation 2, α is the direction of steepest meridian with respect to the nasal–temporal direction and Q_s and Q_f are the asphericity parameters in direction α and direction $\alpha + \pi/2$, respectively, computed by the best fit of the scanning-slit corneal topographer's data. The apex height z_0 is estimated from the value of the BFS radius and the WTW using and basic trigonometric relationships. The surface described by equation 2 reaches the maximum value z_0 at $\rho = 0$. The principal sections of the biconic surface can be oblate ($Q_i > 0$) or prolate ($-1 < Q_i < 0$) ellipses, circumferences ($Q_i = 0$), or parabolas ($Q_i = -1$). Equation 2 may be customized to exclude 1 or 2 asphericity parameters and describe more regular shapes. The construction of the solid model of the cornea also requires the knowledge of extensions of the optical zone and of the peripheral annular zone, the latter given by the WTW distance. The minimum thickness of the optical zone must correspond to the scanning-slit corneal topographer's data, and the distribution of the thickness in the peripheral zone is also taken from the thickness map. The patient-specific solid model is then discretized into 8-node brick finite elements[4] according to the specified mesh size. In the current simulations, the discretized model consists of 2500 nodes and 1740 elements (Figure 1).

Unlike other approaches,[21] this study modeled the cornea only, not the whole eye. Therefore, in this model, the displacement boundary conditions must describe the compliant support offered by the limbus. As discussed in previous studies,[20,22] the limbus does not allow radial expansion of the cornea but only the rotation about the mean circumference of the limbus. In addition, given the stiffness of the limbus structure, the displacements of the mean limbus circumference in the z direction are uniform and do not affect the corneal deformation; therefore, they can be assumed to be null.

Material Model

In the numerical simulations, a corneal material model based on the statistically distributed fiber reinforcement concept was used.[10] The model considered the structurally relevant layer of the cornea (ie, stroma) only; the thinner membranes were disregarded, mainly for lack of information about their mechanical properties. A reversible material behavior was assumed because the eyes in this study did not show degenerative behavior postoperatively. The mechanical behavior of the stroma is described through an anisotropic hyperelastic material, which accounts for a 3-D von Mises–type distribution of the orientation of the collagen fibril families. The strain energy density function Ψ is assumed to be the sum of 3 independent terms with full separation of the arguments as follows:

$$\Psi = \Psi_{vol}(J) + \Psi_{iso}(\bar{I}_1, \bar{I}_2) + \Psi_{aniso}(\bar{I}^*_{4M})$$

The term Ψ_{vol} accounts for the volumetric elastic response and depends on the Jacobian $J = \det \mathbf{F}$, where $\mathbf{F} = d\mathbf{x}/d\mathbf{X}$ is the deformation gradient and det is the symbol for the determinant operator. The term Ψ_{vol} has the function of enforcing the incompressibility constraint and has the operative form

$$\Psi_{vol}(J) = \frac{1}{4}K\left(J^2 - 1 - 2\log J\right)$$

where K is a stiffness coefficient related to the bulk modulus. The term Ψ_{iso} describes the behavior of the isotropic components of the material, and depends on the first and second invariants, $\bar{I}_1$ and $\bar{I}_2$ (Appendix A) of the isochoric Cauchy-Green deformation tensor $\bar{\mathbf{C}} = \bar{\mathbf{F}}^T\bar{\mathbf{F}}$, with $\bar{\mathbf{F}} = J^{-1/3}\mathbf{F}$, according to the Mooney-Rivlin model as follows:

$$\Psi_{iso}(\bar{I}_1, \bar{I}) = \frac{1}{2}\mu_1(\bar{I}_1 - 3) + \frac{1}{2}\mu_2(\bar{I}_2 - 3) \quad (3)$$

where $\mu = \mu_1 + \mu_2$ is the shear modulus of the material. The term Ψ_{aniso} addresses the anisotropic contribution of 2 non-randomly oriented collagen fibrils. A fibril family M is defined in terms of a unit vector field $\mathbf{a}_M$ that identifies the main orientation of the family. The spatial distribution of the fibrils at a point follows the normalized von Mises distribution, characterized by the dispersion coefficient b_M (ρ, θ, z) > 0. The anisotropic strain energy function Ψ_{aniso} used in the model is

$$\Psi_{aniso}(\bar{I}^*_{4M}) = \sum_{M=1}^{2}\frac{1}{2}\frac{k_{1M}}{k_{2M}}\exp\left[k_{2M}(\bar{I}^*_{4M} - 1)^2\right]\left(1 + K^*_M\sigma^2_{I^*_{4M}}\right) \quad (4)$$

where k_{1M} are stiffness parameters and k_{2M} are dimensionless rigidity parameters. Appendix A shows the expressions of the variables in equation 3 and equation 4. The details, properties, and advantages of the chosen material model can be found in the original paper.[10]

The adopted material model requires the definition of 7 material parameters (K, μ_1, μ_2, k_{11}, k_{21}, k_{12}, k_{22}) and the spatial distribution of the main orientation $\mathbf{a}_M$ of the fibrils and of the coefficient b_M (ρ, θ, z) in the entire cornea. An accurate description of the collagen fibrils orientation and density distribution in the human cornea has been discussed,[29,36,37] and it was taken as the basis for the definition of the material model of the human cornea.[10,22] Figure 2 shows the orientation and the dispersion of the fibrils on the anterior surface of the cornea used in the present calculations.

As mentioned, the optimum choice of the material parameters should be based on patient-specific nondestructive in vivo mechanical tests; for example, by applying a short, intense air jet to the center of the cornea and recording the

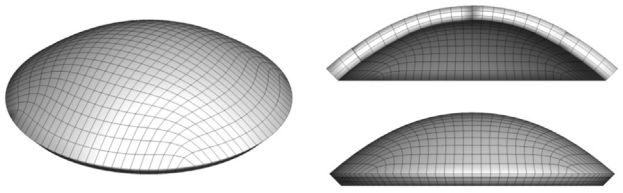

Figure 1. Solid model of one of the human corneas (case 5, right eye) in the physiologic configuration and finite element discretization. *Left*: Top view. *Right, top*: Nasal–temporal meridian section. *Right, bottom*: Nasal–temporal side view. The nodes at the limbus are blocked in the radial direction, and the displacements in the z direction allow rotation of the shell about the central circumference of the limbus.

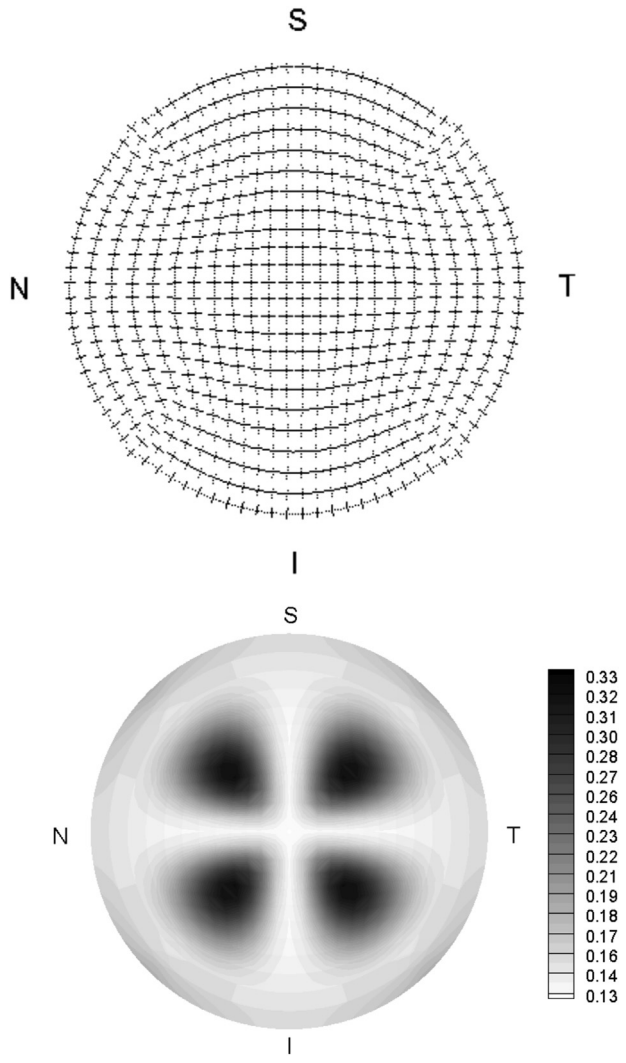

Figure 2. Distribution of the orientation and anisotropy level of the 2 sets of fibers in the top layer of the finite element model of the cornea used in the present calculation. Geometry refers to the right eye of case 5. *Top*: Mean orientation of the fibrils. *Bottom*: Contour level of the scalar variable κ_M (see Appendix B) expressing the level of the anisotropy. The light gray represents strong anisotropy and the dark gray, dominant isotropy (see also Niroomandi et al.[25]).

subsequent deformation of the cornea with imaging systems. Unfortunately, the data considered here did not include mechanical tests but only geometric measurements corresponding to 2 situations; that is, preoperative and postoperative. Therefore, the calibration of the material parameters was performed in 2 steps. First, an initial set of material properties for the chosen material model was calibrated considering the inflation tests on human corneas documented by Bryant and McDonnell.[16] In this phase, geometry of the left eye in case 1 was adopted and fixed boundary conditions at the limbus were used to replicate the experimental conditions. The initial set of calibrated parameters was refined subsequently for each case by evaluating the mechanical response of the patient-specific cornea under physiologic IOP in preoperative geometry and postoperative geometry.

The rationale behind the calibration was as follows: The solid model built with the scanning-slit corneal topographer's data corresponds to the stressed configuration of the cornea, which reacts to the patient-specific IOP. Therefore, the geometry of the solid model to be used in the finite element method should be modified to represent the natural, or stress-free, configuration, corresponding to a zero IOP. The finite-element code used here had a built-in procedure to identify the natural, or unloaded, configuration.[20] Appendix B shows the procedure in brief.

In the present study, it was assumed that the material properties of the stroma do not change after the surgery. However, because the thickness of the shell structure was modified, the structural properties were modified, changing the mechanical response of the cornea. The material properties for the different cases were selected by alternating the simulation of the preoperative and postoperative configurations; the stress-free configuration had to be determined for both. It was assumed that in the stress-free configurations, the geometry of the posterior surface of the cornea must be equal in the preoperative cornea and the postoperative cornea.

Using this procedure, the material properties were calibrated to fit both eyes in case 1. Then, use of the same set of material properties was attempted in all the other cases. In 2 cases, the results were acceptable and the 2 cases were grouped with case 1. In 2 other cases, the code did not converge during the iterative procedure used for the identification of the stress-free configuration. The missing convergence of the nonlinear procedure signals instability of the corneal shell structure. This means that for particular geometries of the cornea, the material must be characterized by stiffer values of the parameters connected with the isotropic behavior. The isotropic components provide support at low IOP values, when the collagen fibrils are not yet recruited. Therefore, a new set of material properties had to be chosen to fit the behavior of the eyes in the last 2 cases. This rather costly procedure provided the stress-free geometry and material properties.

This procedure calibrated the model to inflation data in the range of 0 to 16 mm Hg only, which could lead to nonunique parameters that control properties at higher strain levels. This point should be considered when the model is be applied in the simulation of surgical procedures other than PRK that can cause local stress concentrations (eg, arcuate incisions or intracorneal stromal ring segments).

After the identification of the stress-free configuration and of the set of material parameters for each case under study, a quasistatic analysis under increasing IOP (0 to 40 mm Hg) was performed. The analysis provided information on the displacement and stress fields at different IOPs.

Plots of the IOP of versus the apical displacement provide useful synthesis of the results of an experimental or numerical analysis under increasing IOP. Changes in the apex elevation and curvature of the cornea at different IOPs imply changes in the refractive power of the cornea. The code used in this study computed the local refractive power along any meridian considering the central 3.0 mm zone and using equation 1.

The cornea shell is in a tensile state, and in normal conditions the highest stresses are in the central region. For the cases in this study, the nasal–temporal and superior–inferior components of the Cauchy stress at the physiologic IOP of 16 mm Hg were evaluated at the center of the cornea, close

Table 1. Geometric eye parameters provided by the scanning-slit topographer for the 10 preoperative cases.

Case/Eye	BSF^{ant} (mm)	BFS^{pos} (mm)	WTW (mm)	t_{apex} (μm)	t_{limbus} (μm)	R_f (mm)	R_f^{sf} (mm)	R_s (mm)	R_s^{sf} (mm)	z_0 (mm)	α (°)
1/L	8.01	6.55	11.6	561	668	7.755	7.484	7.537	7.437	2.486	80
1/R	8.03	6.57	11.6	562	692	7.839	7.572	7.616	7.514	2.477	89
2/L	7.95	6.62	12.3	538	690	7.654	7.752	7.562	7.787	2.912	59
2/R	7.87	6.58	12.4	544	660	7.649	7.748	7.541	7.777	3.023	122
3/L	8.06	6.58	11.6	563	673	7.696	7.739	7.587	7.780	2.463	86
3/R	7.86	6.38	11.3	562	702	7.468	7.619	7.439	7.529	2.396	18
4/L	7.98	6.53	11.6	541	682	7.850	7.908	7.565	7.787	2.499	83
4/R	8.04	6.60	11.6	554	675	7.877	7.939	7.667	7.885	2.472	84
5/L	7.77	6.13	11.0	538	653	7.067	6.859	6.924	6.870	2.282	101
5/R	7.64	6.24	11.1	541	636	7.232	7.277	7.096	7.290	2.390	87

α = cylinder angle; BFS^{pos} = best fitting curvature radius for the posterior surface; BSF^{ant} = best fitting curvature radius for the anterior surface; R_f = flattest curvature radius; R_f^{sf} = flattest curvature radius for the stress free configuration; R_s = steepest curvature radius; R_s^{sf} = steepest curvature radius for the stress free configuration; t_{apex} = thickness at the apex; t_{limbus} = average thickness at the limbus; WTW = white-to-white distance; z_0 = elevation at apex

to the anterior surface and posterior surface for the preoperative and postoperative configurations.

Built-in Reprofiling Procedure

The second goal was the patient-specific verification of a numerical reprofiling procedure[20] implemented in the finite-element code. By automatically remodeling the anterior surface of the numerical cornea according to the expected final profile, one can predict the mechanical and optical outcomes of a planned refractive surgery. A PRK intervention is controlled by the spherical correction and cylindrical correction that will provide the desired corneal refraction. The surgeon carefully chooses these data on the basis of examination of the patient's eye, and the surgical instrumentation is programmed to follow a patient-specific ablation pattern. In cylindrical coordinates, an ablation pattern is described by a continuous non-negative function $z = f(\rho, \theta)$, where ρ is the distance from the corneal apex and θ is the angle with respect to the nasal–temporal direction. Ablation patterns are designed in 2 regions; that is, the optical zone (ie, central zone where the refractive correction is accurately planned) and the transition zone, characterized by a smooth and continuous change in curvature between the treated regions and the untreated regions.[28,38–40] The intervention is irreversible, and when there are irregularities in the corneal geometry or of anomalies in the stromal tissue, the actual outcomes of a planned ablation might be unpredictable.

In the finite-element code used here, a procedure was implemented that modifies the anterior surface of a preoperative cornea according to the planned ablation[20] and for IOP in the physiologic range, computes the corneal geometry, the refractive power, and the distribution of the stresses in the stroma. The input of the built-in reprofiling procedure are the radius of the ablated zone and the standard data used in the refractive surgery; that is, the power correction P_c through the following fundamental parameters: the spherical correction S_c, the cylindrical correction C_c at the assigned angle α_c with respect to the nasal–temporal direction:

$$P_c = S_c + C_c \times \alpha_c$$

The ablation patterns implemented in the code obey the Munnerlyn equation[41] in axisymmetric cases or a profile described by the difference in 2 biconic surfaces in astigmatic cases. Details of the reprofiling equations and their theoretical derivation are described Pandolfi et al.[20]

Table 2. Geometric eye parameters provided by the scanning-slit topographer for the 10 postoperative cases.

Case/Eye	BSF^{ant} (mm)	BFS^{pos} (mm)	WTW (mm)	t_{apex} (μm)	t_{limbus} (μm)	R_f (mm)	R_f^{sf} (mm)	R_s (mm)	R_s^{sf} (mm)	z_0 (mm)	α (°)
1/L	8.24	6.58	11.6	492	668	8.365	8.065	7.907	7.820	2.387	100
1/R	8.35	6.53	11.6	459	692	8.666	8.669	8.320	8.482	2.343	98
2/L	8.09	6.60	12.5	501	690	8.046	8.183	7.943	8.121	2.953	83
2/R	7.99	6.56	12.4	492	660	8.005	7.731	7.821	7.732	2.950	150
3/L	8.18	6.42	11.4	491	673	8.139	8.161	7.949	8.116	2.313	103
3/R	8.05	6.36	11.3	520	702	7.973	8.008	7.889	8.059	2.316	96
4/L	8.35	6.55	11.7	456	682	8.268	8.322	8.055	8.260	2.392	85
4/R	8.24	6.53	11.6	462	675	8.229	8.282	8.000	8.203	2.387	92
5/L	7.93	6.10	11.0	501	653	7.325	7.364	7.199	7.379	2.217	104
5/R	7.75	6.19	11.1	492	636	7.576	7.604	7.382	7.556	2.341	95

α = cylinder angle; BFS^{pos} = best fitting curvature radius for the posterior surface; BSF^{ant} = best fitting curvature radius for the anterior surface; R_f = flattest curvature radius; R_f^{sf} = flattest curvature radius for the stress free configuration; R_s = steepest curvature radius; R_s^{sf} = steepest curvature radius for the stress free configuration; t_{apex} = thickness at the apex; t_{limbus} = average thickness at the limbus; WTW = white-to-white distance; z_0 = elevation at apex

Table 3. The 2 sets of material parameters identified in the 10 eyes.

Group	Cases	K (MPa)	μ_1 (MPa)	μ_2 (MPa)	k_{11} (MPa)	k_{21}	k_{12} (MPa)	k_{22}
Group 1	1, 3, 5	5.5	0.06	−0.01	0.04	200	0.04	200
Group 2	2, 4	5.5	0.09	−0.02	0.04	200	0.04	200

K = bulk modulus; k_{11} = first fiber family stiffness; k_{12} = first fiber family rigidity; k_{21} = second fiber family stiffness; k_{22} = second fiber family rigidity; μ_1 = first shear modulus; μ_2 = second shear modulus

RESULTS

The study comprised 10 eyes of 5 patients. Table 1 and Table 2 show the stress-free curvatures for the preoperative geometry and postoperative geometry, respectively. Table 3 shows the material properties for the 2 material groups. Table 4 shows the refractive data related to the PRK procedure in the 10 cases. The ablation profiles applied for the numerical procedure were described by biconic surfaces in 6 cases and by ellipsoidal surfaces in the remaining 4 cases.

Figure 3, *A*, and Figure 3, *B*, show the mean IOP–apical displacement curve ± the standard deviation (SD) in the 2 material groups computed for the preoperative configuration and the postoperative configuration, respectively. The mean maximum apical displacement in the 10 cases was 0.377 mm ± 0.008 (SD) preoperatively and 0.404 ± 0.019 mm postoperatively; this represents a 7% increase from preoperative to postoperative. The built-in reprofiling procedure produced results similar to those obtained directly using the scanning-slit corneal topographer data in postoperative eyes. Figure 3, *C*, shows the plot of the mean IOP versus the apical displacement obtained through numerical simulations with reference to the preoperative response, the postoperative response, and the prediction of the built-in reprofiling procedure in material Group 1. Figure 3, *D*, shows these results in material Group 2.

The refractive power predicted by the built-in reprofiling procedure was close to the refractive power numerically computed for the postoperative geometry (Table 5). In the 10 cases, the mean difference between the prediction of the built-in reprofiling procedure and the postoperative simulation in the refractive power was 1.2% ± 1.4% in the nasal–temporal meridian and 1.9% ± 1.2% in the superior–inferior meridian.

In some cases, the agreement in the results of the built-in reprofiling procedure and the postoperative analysis was particularly high. For the left eye in case 4, Figure 4 compares the numerical response for the preoperative cornea, the postoperative cornea, and the prediction of the built-in reprofiling procedure for the apical displacement and the refractive power along the nasal–temporal meridian.

Tables 6 shows the anterior and posterior corneal surface stresses in the preoperative configuration in each case, and Table 7 shows the values in the postoperative configuration. Figure 5 shows the mean numerically evaluated Cauchy stress components (in kPa) at the center of the anterior surface and posterior surface of the cornea. The maximum postoperative stress on the anterior surface increased by 20% over the preoperative stress, and the SD showed a 150% increase. The increase in the mean stress on the posterior surface was less marked (approximately 10%), with a 16% increase in the SD.

For the highest refractive correction considered in the study (right eye, case 1), Figure 6 shows the distribution of the Cauchy stress component in the nasal–temporal direction on the anterior surface of the cornea at the physiologic IOP and compares the outcomes of the preoperative, postoperative, and reprofiling analyses. The color maps vary between null stress (*blue*) to 22 kPa (*red*). The estimated postoperative increase in the nasal–temporal and

Table 4. Refractive power difference between preoperative configuration and postoperative configuration evaluated from corneal topographies and the spherical correction and cylindrical correction used in the reprofiling simulations.

Case/Eye	$\Delta RP^{NT}{}_c$ (D)	$\Delta RP^{SI}{}_c$ (D)	Δt (μm)	S_c (D)	C_c (D)	α_c (°)
1/L	−3.33	−2.26	69	2.26	1.07	10
1/R	−5.84	−5.63	103	5.63	0.21	0
2/L	−2.21	−2.25	37	2.21	—	—
2/R	−0.47	−0.39	52	0.39	—	—
3/L	−2.29	−1.83	72	1.83	0.47	0
3/R	−2.56	−3.09	42	2.56	0.53	100
4/L	−2.44	−2.89	85	2.44	0.45	80
4/R	−2.20	−2.14	92	2.14	—	—
5/L	−2.76	−2.83	37	2.76	—	—
5/R	−2.28	−1.90	49	1.90	0.38	0

α_c = angle refractive correction used to simulate surgery with numerical reprofiling; C_c = cylindrical refractive correction used to simulate surgery with numerical reprofiling; S_c = spherical refractive correction used to simulate surgery with numerical reprofiling; $\Delta RP^{NT}{}_c$ = change in refractive power in the nasal–temporal direction; $\Delta RP^{SI}{}_c$ = change in refractive power in the superior–inferior direction; Δt = change in thickness (ie, decrease)

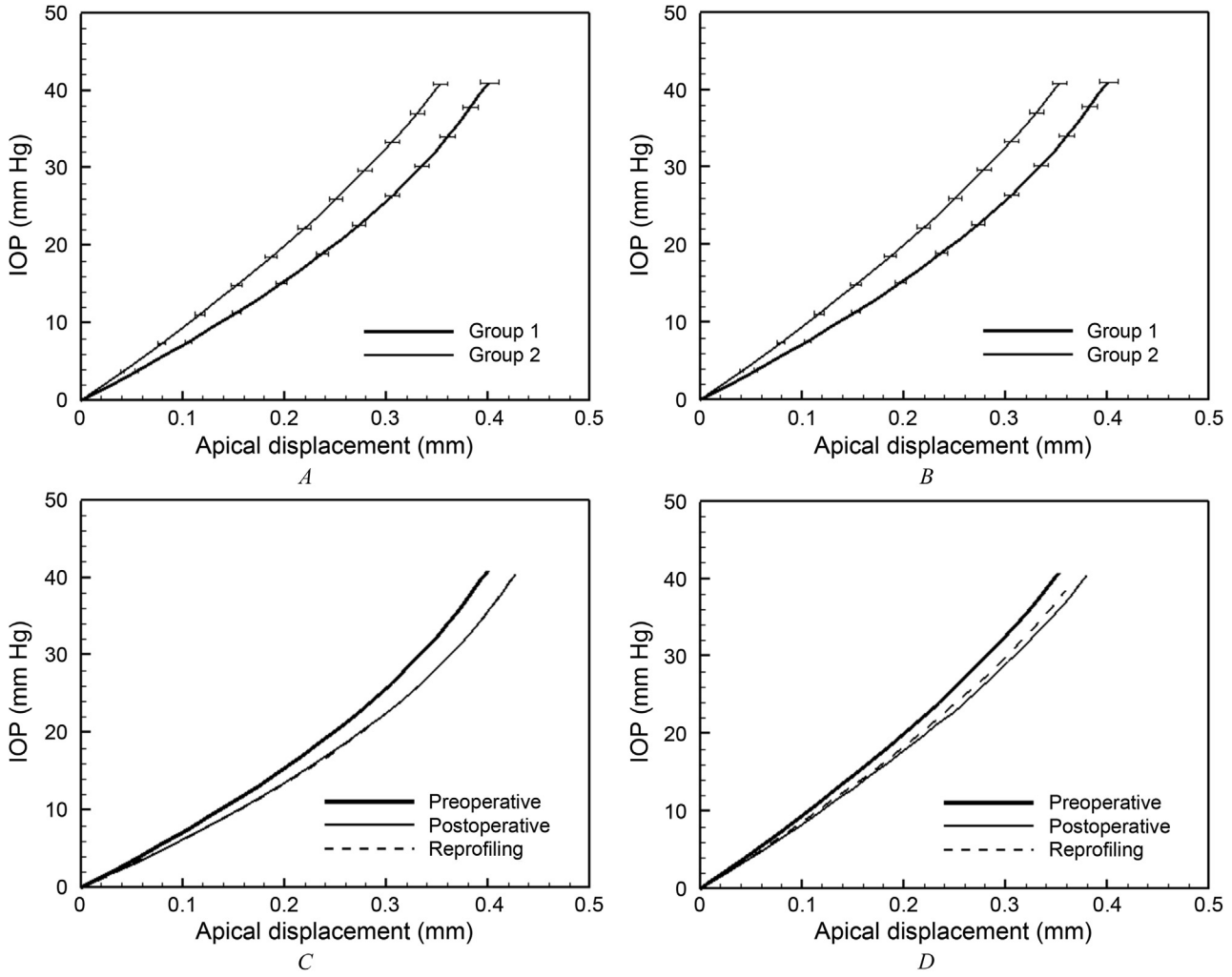

Figure 3. Numerically computed IOP versus apical displacement curves. *A*: Mean response of the preoperative eyes by material group. *B*: Mean response of the postoperative eyes by material groups. *C*: Mean responses for eyes of material Group 1. *D*: Mean responses for eyes of material Group 2 (IOP = intraocular pressure).

superior–inferior stresses on the anterior surface was approximately 47% in the postoperative analysis and the reprofiling analysis.

DISCUSSION

We present a quasistatic analysis of the mechanical response of 10 human corneas before and after PRK. The simulations were performed using an ad hoc finite-element code able to account for all the geometrical and material nonlinearities typical of biologic organs. They also included procedures to identify the stress-free (or natural) configuration of the cornea and to mimic the PRK reprofiling of the anterior surface of the cornea.

The numerical analyses predicted the biomechanical and optical outcomes of PRK. In particular, the numerical calculations estimated the postoperative refractive power along any meridian and the stress distribution in the cornea model. The mechanical response consists of the displacement and the strain field, which are direct outputs of the numerical analyses. From the strain field, the material model provided the stress field within the cornea.

The displacement field describes the motion of the cornea under the action of IOP. Because of the elasticity, the apical displacement increases with increasing IOP, and this effect is more evident when the material is more compliant (softer) and when the cornea is thinner. The numerical analyses clearly showed that the corneal thinning caused by PRK increased the compliance of the corneas and their sensitivity to IOP.

The apical displacement predictions of the reprofiling procedure were reasonably good with respect to the calculation of the postoperative geometry. The

Table 5. Percentage difference between the refractive power provided by the built-in reprofiling procedure and the refractive power numerically computed for the postoperative configuration at an IOP of 16 mm Hg.

	Meridian	
Case/Eye	N–T	S–I
1/L	3.4	5.0
1/R	3.3	0.2
2/L	−0.7	2.7
2/R	1.2	1.3
3/L	1.5	2.5
3/R	2.3	1.3
4/L	−0.2	1.6
4/R	−0.5	2.3
5/L	0.2	1.6
5/R	1.2	0.9

N–T = nasal–temporal; S–I = superior–inferior

differences in the apical displacement were, in general, below 1%, and the few cases in which the differences were larger had an ablation profile that was described by a biconic equation. The comparison between surgical outcomes and built-in procedure predictions for eyes in material Group 1 was excellent. The prediction of the built-in procedure was less precise for the eyes in Group 2. A reason for the discrepancy might be that for 3 of 4 eyes in Group 2, we disregarded in the reprofiling procedure the small cylindrical correction (<0.5 D) that was included in the actual surgery. We did this because in terms of refractive power, the numerical reprofiling procedure provided results worse than the ones obtained with the spherical correction only. Thus, the numerically reprofiled corneas were thicker and stiffer than the postoperative ones. In limiting the refractive power error, we obtained a larger error on the apical displacement. The large differences that appear in some cases also occurred because the ablation profile used in the built-in reprofiling procedure was not the same as that used by the excimer laser. The information about the actual ablation profile was not available to us; we knew the basic correction parameters only. In terms of applying the proposed numerical procedure in clinical practice, the exact ablation profile that will be used for the patient must be considered.

Apical displacement is a convenient parameter for a statistical analysis. Although it alone cannot guarantee the predictability of a model, when combined with the 2 curvatures along superior–inferior and nasal–temporal meridian, it can be considered acceptable in describing the numerical outcomes of simulations of individual cases. The increase in forward

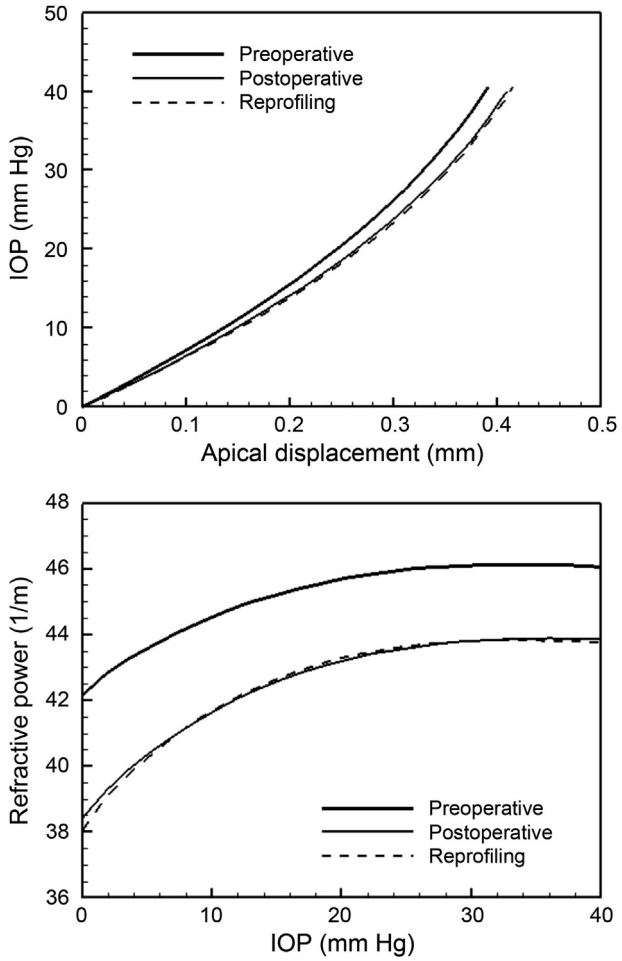

Figure 4. Numerical results for the left eye of case 5. Local refractive power evaluated in the central 3.0 mm (IOP = intraocular pressure).

displacement of the apex implies a small reduction in local curvature and a reduction in the planned correction for myopia. Therefore, the optical outcomes of PRK depend not only on the ablation profile but also on the mechanical response of the system. This secondary effect may explain the undercorrection or overcorrection that can occur during refractive surgery. Figure 4, *top*, shows that the refractive power in the central 3.0 mm was modified slightly by the IOP, although the value of the refractive power was rather stable in the range of the physiologic IOP. In addition, as Figure 4, *bottom*, shows, the postoperative refractive power was more sensitive to IOP changes than the preoperative refractive power. This was clearly seen with low IOP and was the result of the higher compliance of a thinner cornea.

Another important consequence of the refractive surgery that is not yet sufficiently considered in the common practice is the increase in stress inside the cornea. Numerical calculations provide an

Table 6. Anterior and posterior corneal surface stresses (kPa) in the preoperative condition.

	Corneal Surface Stress					
	Nasal–Temporal		Superior–Inferior		von Mises	
Case/Eye	Anterior	Posterior	Anterior	Posterior	Anterior	Posterior
1/L	14.8	10.7	14.8	10.8	21.0	16.1
1/R	15.2	10.2	15.1	10.2	21.6	15.7
2/L	15.2	14.9	15.1	14.8	21.5	21.1
2/R	14.3	14.6	14.2	14.5	20.2	20.7
3/L	16.6	9.4	16.5	9.3	23.9	15.8
3/R	16.3	8.4	16.3	8.4	23.7	15.4
4/L	17.2	11.5	17.0	11.5	24.3	17.6
4/R	15.9	9.8	15.7	9.7	22.6	15.5
5/L	16.7	11.5	16.6	11.4	23.6	17.4
5/R	17.1	11.0	16.9	10.9	24.2	17.1
Mean ± SD	15.9 ± 1.0	11.2 ± 2.0	15.8 ± 0.9	11.2 ± 2.0	22.7 ± 1.4	17.2 ± 2.0

estimate of the stress field; the accuracy of these calculations depends strongly on the material and geometrical models chosen. The corneal shell is in a tensile stress state and under normal conditions, the highest stress is in the central region. The knowledge of the preoperative stress and postoperative stress is of paramount importance to understand the possible damage to corneal tissue induced by refractive surgery. Given the particular microstructure of the cornea described in Figure 2, the most significant stress components are the horizontal (nasal–temporal) and vertical (superior–inferior) Cauchy stress components at the center of the cornea under physiologic IOP. The highest value and lowest value are close to the anterior surface and posterior surface, respectively. A comparison of these stress components between the preoperative configuration and the postoperative configuration found a mean increase of approximately 20%, with peaks of 47% for the deepest ablation (left eye in case 1). In this case, we compared the distribution of the nasal–temporal components of Cauchy stress on the anterior surface between the preoperative state, postoperative state, and reprofiling state. The postoperative maps were characterized by higher stress in the central zone of the cornea. The difference in the stress maps was also seen between the postoperative state and the reprofiling state. Again, such differences might have been related to the different equations of the ablation profiles actually used in the surgical procedure with respect to the ones used in our code.

Table 7. Anterior and posterior corneal surface stresses (kPa) in the postoperative condition.

	Corneal Surface Stress					
	Nasal–Temporal		Superior–Inferior		von Mises	
Eye/Case	Anterior	Posterior	Anterior	Posterior	Anterior	Posterior
1/L	20.3	12.7	20.1	12.7	29.0	19.9
1/R	22.3	10.5	22.3	10.5	33.1	19.8
2/L	15.7	15.0	15.6	14.9	22.0	21.2
2/R	15.2	16.8	15.2	16.8	21.7	24.0
3/L	22.1	10.9	21.9	10.8	32.2	19.7
3/R	19.9	8.7	19.8	8.6	29.3	17.8
4/L	22.6	14.1	22.4	14.1	32.3	21.8
4/R	20.7	12.3	20.5	12.2	29.6	19.5
5/L	18.3	10.2	18.1	10.1	26.2	17.1
5/R	20.0	11.8	19.8	11.7	28.6	19.0
Mean ± SD	19.7 ± 2.5	12.3 ± 2.3	19.6 ± 2.3	12.2 ± 2.3	28.4 ± 3.8	20.0 ± 1.9

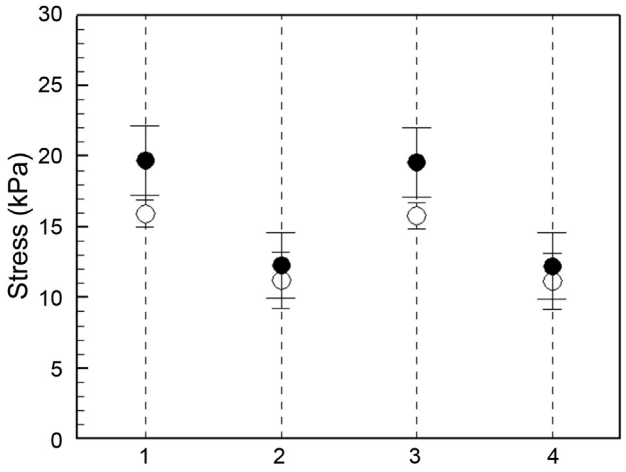

Figure 5. Numerically evaluated average Cauchy stress components and SDs at the center of the anterior surface and posterior surfaces of the cornea. Horizontal axis labels refer to the (1) nasal–temporal stress component on the anterior surface, (2) nasal–temporal stress component on the posterior surface, (3) superior–inferior stress component on the anterior surface, and (4) superior–inferior stress component on the posterior surface. White circles and black circles denote preoperative stress and postoperative stress, respectively.

The orientation of the collagen fibrils in the cornea varies with the depth.[30] In the posterior cornea, lamellae follow the cornea curvature, while near the anterior surface, a portion of the lamella fibrils is inclined up to ± 3.5 degrees with respect to the anterior surface.[42] In the central part, the fibrils are preferentially oriented in the superior–inferior and nasal–temporal directions, and near the limbus they run circumferentially. There is no clear evidence of the presence of sets of fibrils subparallel to the cornea surfaces and orthogonal to the limbus. Our microstructural model of the cornea can be improved; for example, by using an alternative material model that respects the microstructure of the posterior cornea and describes the distribution of the fibrils tangential to the corneal surface, by considering a depth-dependent distribution of the orientation of the fibrils, and by developing a new description of the limbus microstructure in which the circumferential and radial fibrils are differentiated to match the experimental observations.

Other improvements are related to the postprocessing of the numerical results. A stronger demonstration of the comparison between the built-in reprofiling procedure and the postoperative configuration can be inferred by evaluating the values of the sphere and cylinder of the model as function of the IOP in the physiologic range. Although this feature is not yet available, we plan to implement it in the code in the near future.

In conclusion, stress analysis of the human cornea can be a valuable aid in determining the possible concentration of stress caused by refractive surgery. Population studies of ocular biomechanics modeling give a better idea about the predictability of the model and approach. The inverse-analysis approach is a good way of estimating material properties within an acceptable limit of error. As mentioned, to implement patient-specific models as a surgical prediction tool, the present approach must be supported by in vivo mechanical tests from in which the material properties of the corneal tissue can be evaluated. If such properties become available, the built-in reprofiling procedure

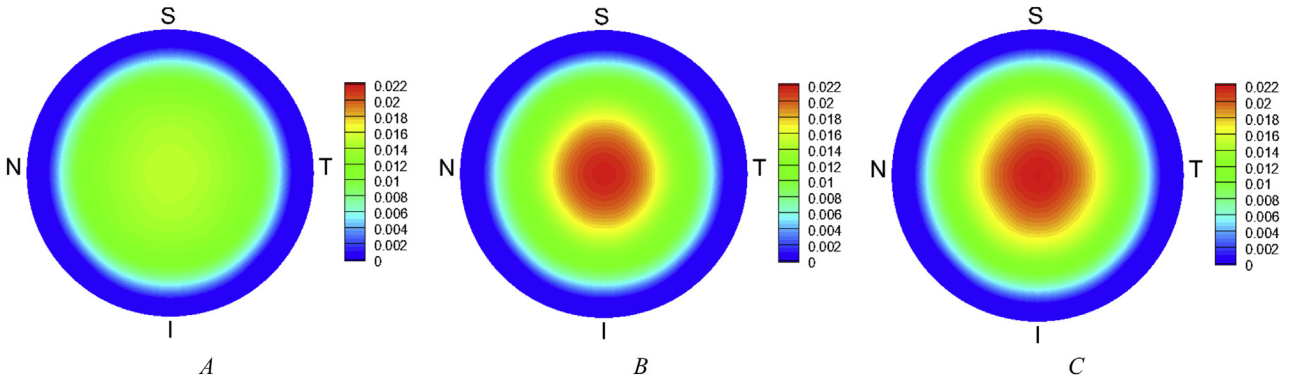

Figure 6. Numerical results for the left eye in case 1, the highest correction considered. Contour levels of the nasal–temporal component of the Cauchy stress in MPa on the anterior surface of the cornea. *A*: Preoperative stress distribution. *B*: Postoperative stress distribution evaluated from the scanning-slit corneal topographer maps. *C*: Postoperative stress distribution prediction of the reprofiling procedure.

will be able to predict postoperative stress distribution and to identify situations in which PRK can lead to permanent damage of the corneal tissue.

WHAT WAS KNOWN

- Finite-element simulations of refractive corneal surgery based on reliable geometric and material models of the cornea provide estimates of the biomechanical behavior of the stroma undergoing laser ablation reprofiling.

WHAT THIS PAPER ADDS

- Using preoperative and postoperative geometry of 10 corneas having PRK, a calibration procedure was able to identify the patient-specific material properties of the cornea.
- Use of a patient-specific numerical model of corneal PRK provided a quantitative estimate of the biomechanical behavior of the cornea, including the refractive outcomes and the variation in stress within the cornea.
- Accurate multiparameters material models of the cornea are available; however, the calibration of their parameters requires the comparison of 2 or more configurations corresponding to different loadings or to different geometries (eg, thickness).

APPENDIX A

The first and second invariant of the isochoric Cauchy-Green deformation tensor are defined as

$$\bar{I}_1 = \mathrm{tr}\overline{\mathbf{C}} \quad \bar{I}_2 = \frac{1}{2}\left[\left(\mathrm{tr}\overline{\mathbf{C}}\right)^2 - \mathrm{tr}\left(\overline{\mathbf{C}}\right)^2\right]$$

The two pseudo-invariants $\bar{I}^*_{4\mathrm{M}}(\mathrm{M} = 1,2)$ are defined as

$$\bar{I}^*_{4\mathrm{M}} = \mathbf{H}_\mathrm{M} : \overline{\mathbf{C}}$$

The structure tensor $\mathbf{H}_\mathrm{M}$ is defined as

$$\mathbf{H}_\mathrm{M} = \kappa_\mathrm{M}\mathbf{I} + (1-3\kappa_\mathrm{M})\mathbf{a}_\mathrm{M} \otimes \mathbf{a}_\mathrm{M}$$

where $\mathbf{I}$ is the identity tensor. The scalar parameter κ_M depends on the chosen spatial distribution of the fibrils orientation b_M (ρ, θ, z). The 2 terms

$$K^*_\mathrm{M} = k_{2\mathrm{M}} + 2\mathrm{k}^2_{2\mathrm{M}}\left(\bar{I}^*_{4\mathrm{M}} - 1\right)^2$$

and

$$\sigma^*_{I_{4\mathrm{M}}} = \overline{\mathbf{C}} : <\mathbf{A}_\mathrm{M} \otimes \mathbf{A}_\mathrm{M}> : \overline{\mathbf{C}} - \left(\mathbf{H}_\mathrm{M} : \overline{\mathbf{C}}\right)^2$$

are introduced to include in the material model the variance of the fibril orientation distribution.

APPENDIX B

The initially assigned coordinates $\mathbf{x}$ of the numerical model are the sum of the unknown stress free coordinates $\mathbf{X}^0$ and the nodal displacement $\mathbf{u}$ due to application of the IOP; that is

$$\mathbf{x} = \mathbf{X}^0 + \mathbf{u}$$

The procedure begins by assuming

$$\mathbf{X}^0 = \mathbf{x}$$

Then the code performs an iterative sequence of static analyses consisting in applying a progressively increasing pressure on the posterior side of the shell up to the physiological IOP. At the end of the *k*-th iteration, the computed nodal displacements $\mathbf{u}^k$ are used for a new estimate $\mathbf{X}^k$ of the stress-free coordinates as

$$\mathbf{X}^k = \mathbf{x} - \mathbf{u}^k$$

The procedure is interrupted when the norm of the difference between the coordinates of 2 iterations becomes smaller than a prescribed tolerance $\varepsilon = 10^{-6}$:

$$\left|\mathbf{X}^k - \mathbf{X}^{k-1}\right| \leq \varepsilon\left|\mathbf{X}^{k-1}\right|$$

Thus, the code performs a best fit of the stress-free anterior and posterior geometry with the biconic equations and the stress-free optimum, parameters of the cornea are computed.

REFERENCES

1. Lapid-Gortzak R, van der Linden JW, van der Meulen IJE, Nieuwendaal CP. Advanced personalized nomogram for myopic laser surgery: first 100 eyes. J Cataract Refract Surg 2008; 34:1881–1885
2. Moshirfar M, Simpson RG, Dave SB, Christiansen SM, Edmonds JN, Culbertson WW, Pascucci SE, Sher NA, Cano DB, Trattler WB. Sources of medical error in refractive surgery. J Refract Surg 2013; 29:303–310
3. Pinsky OM, van der Heide D, Chernyak D. Computational modeling of mechanical anisotropy in the cornea and sclera. J Cataract Refract Surg 2005; 31:136–145
4. Pandolfi A, Manganiello F. A model for the human cornea: constitutive formulation and numerical analysis. Biomech Model Mechanobiol 2006; 5:237–246
5. Nguyen TD, Jones RE, Boyce BL. A nonlinear anisotropic viscoelastic model for the tensile behavior of the corneal stroma. J Biomechan Eng 2008; 130:041020
6. Raghupathy R, Barocas VH. A closed-form structural model of planar fibrous tissue mechanics. J Biomechan 2009; 42:1424–1428
7. Girard MJA, Downs JC, Burgoyne CF, Suh J-KF. Peripapillary and posterior scleral mechanics–part I: development of an anisotropic hyperelastic constitutive model. J Biomechan Eng 2009; 131:051011
8. Gouget CLM, Girard MJ, Ethier CR. A constrained von Mises distribution to describe fiber organization in thin soft tissues. Biomech Model Mechanobiol 2012; 11:475–482. Available at: http://www.bioeng.nus.edu.sg/ivb/publications/A_Constrained_Von_Mises_Distribution_To_Describe_Fiber_Organization_In_Thin_Soft_Tissues.pdf. Accessed March 18, 2014
9. Alastrué V, Martinez MA, Menzel A, Doblaré M. On the use of non-linear transformations for the evaluation of anisotropic rotationally symmetric directional integrals. Application to the stress

analysis in fibred soft tissues. Int J Numer Method Eng 2010; 79:474–504
10. Pandolfi A, Vasta M. Fiber distributed hyperelastic modeling of biological tissues. Mech Mater 2012; 44:151–162
11. Grytz R, Meschke G. A computational remodeling approach to predict the physiological architecture of the collagen fibril network in corneo-scleral shells. Biomech Model Mechanobiol 2010; 9:225–235
12. Nguyen TD, Boyce DL. An inverse finite element method for determining the anisotropic properties of the cornea. Biomechan Model Mechanobiol 2011; 10:323–337
13. Asejczyk-Widlicka M, Śródka W, Schachar RA, Pierścionek BK. Material properties of the cornea and sclera: A modelling approach to test experimental analysis. J Biomechan 2011; 44:543–546
14. Sinha Roy A, Dupps WJ Jr. Patient-specific modeling of corneal refractive surgery outcomes and inverse estimation of elastic property changes. J Biomech Eng 2011; 133:011002
15. Studer HP, Riedwyl H, Amstutz CA, Hanson JVM, Büchler P. Patient-specific finite-element simulation of the human cornea: a clinical validation study on cataract surgery. J Biomechan 2013; 46:751–758
16. Bryant MR, McDonnell PJ. Constitutive laws for biomechanical modeling of refractive surgery. J Biomechan Eng 1996; 118:473–481
17. Cabrera Fernández D, Niazy AM, Kurtz RM, Djotyan GP, Juhasz T. Finite element analysis applied to cornea reshaping. J Biomed Opt 2005; 10:064018
18. Gefen A, Shalom R, Elad D, Mandel Y. Biomechanical analysis of the keratoconic cornea. J Mech Behav Biomed Mater 2009; 2:224–236
19. Alastrué V, Calvo B, Peña E, Doblaré M. Biomechanical modeling of refractive corneal surgery. J Biomech Eng 2006; 128:150–160
20. Pandolfi A, Fotia G, Manganiello F. Finite element simulations of laser refractive corneal surgery. Engineering With Computers 2009; 25:15–24. Available at: http://www.stru.polimi.it/home/pandolfi/WebPage/j-2009-refractive.pdf. Accessed March 18, 2014
21. Roy AS, Dupps WJ Jr. Effects of altered corneal stiffness on native and postoperative LASIK corneal biomechanical behavior: a whole-eye finite element analysis. J Refract Surg 2009; 25:875–887
22. Pandolfi A, Holzapfel GA. Three-dimensional modeling and computational analysis of the human cornea considering distributed collagen fibril orientations. J Biomech Eng 2008; 130:061006
23. Elsheikh A. Finite element modeling of corneal biomechanical behavior. J Refract Surg 2010; 26:289–300
24. Lanchares E, Calvo B, Cristóbal JA, Doblaré M. Finite element simulation of arcuates for astigmatism correction. J Biomech 2008; 41:797–805
25. Niroomandi S, Alfaro I, González D, Cueto E, Chinesta F. Real-time simulation of surgery by reduced-order modeling and X-FEM techniques. Int J Numer Method Biomed Eng 2012; 28:574–588
26. Pandolfi A, Boschetti F. The influence of the geometry of the porcine cornea on the biomechanical response of inflation tests. Comput Methods Biomech Biomed Eng 2013 Mar 22 [Epub ahead of print]
27. Śródka W, Iskander DR. Optically inspired biomechanical model of the human eyeball. J Biomed Opt 2008; 13:044034
28. Cano D, Barbero S, Marcos S. Comparison of real and computer-simulated outcomes of LASIK refractive surgery. J Opt Soc Am A Opt Image Sci Vis 2004; 21:926–936
29. Boote C, Dennis S, Meek KM. Spatial mapping of collagen fibril organisation in primate cornea—an x-ray diffraction investigation. J Struct Biol 2004; 146:359–367
30. Petsche SJ, Pinsky PM. The role of 3-D collagen organization in stromal elasticity: a model based on X-ray diffraction data and second harmonic-generated images. Biomech Model Mechanobiol 2013; 12:1101–1113
31. Cairns G, Ormonde SE, Gray T, Hadden OB, Morris T, Ring P, McGhee CNJ. Assessing the accuracy of Orbscan II post-LASIK: apparent keratectasia is paradoxically associated with anterior chamber depth reduction in successful procedures. Clin Exp Ophthalmol 2005; 33:147–152
32. Ha BJ, Kim SW, Kim SW, Kim EK, Kim T-I. Pentacam and Orbscan II measurements of posterior corneal elevation before and after photorefractive keratectomy. J Refract Surg 2009; 25:290–295
33. Cheng ACK, Ho T, Lau S, Lam DSC. Evaluation of the apparent change in posterior corneal power in eyes with LASIK using Orbscan II with magnification compensation. J Refract Surg 2009; 25:221–228
34. Cheng ACK, Rao SK, Lam DSC. Accuracy of Orbscan II in the assessment of posterior curvature in patients with myopic LASIK. J Refract Surg 2007; 23:677–680
35. Quisling S, Sjoberg S, Zimmerman B, Goins K, Sutphin J. Comparison of Pentacam and Orbscan IIz on posterior curvature topography measurements in keratoconus eyes. Ophthalmology 2006; 113:1629–1632
36. Aghamohammadzadeh H, Newton RH, Meek KM. X-ray scattering used to map the preferred collagen orientation in the human cornea and limbus. Structure 2004; 12:249–256
37. Boote C, Dennis S, Newton RH, Puri H, Meek KM. Collagen fibrils appear more closely packed in the prepupillary cornea: optical and biomechanical implications. Invest Ophthalmol Vis Sci 2003; 44:2941–2948. Available at: http://www.iovs.org/content/44/7/2941.full.pdf. Accessed March 18, 2014
38. Schwiegerling J, Snyder RW. Custom photorefractive keratectomy ablations for the correction of spherical and cylindrical refractive error and higher-order aberration. J Opt Soc Am A Opt Image Sci Vis 1998; 15:2572–2579
39. MacRae S. Excimer ablation design and elliptical transition zones. J Cataract Refract Surg 1999; 25:1191–1197
40. Schwiegerling J, Snyder RW, MacRae SM. Optical aberrations and ablation pattern design. In: MacRae SM, Krueger RR, Applegate RA, eds, Customized Corneal Ablation: the Quest for SuperVision. Thorofare NJ, Slack, 2001; 95–107
41. Munnerlyn CR, Koons SJ, Marshall J. Photorefractive keratectomy: a technique for laser refractive surgery. J Cataract Refract Surg 1988; 14:46–52
42. Winkler M, Shoa G, Xie Y, Petsche SJ, Pinsky PM, Juhasz T, Brown DJ, Jester JV. Three-dimensional distribution of transverse collagen fibers in the anterior human corneal stroma. Invest Ophthalmol Vis Sci 2013; 54:7293–7301